Spectroscopic Characterization and Systematic Crystal-Field Modeling of Optically Active Rare Earth R^{3+} Ions in the Bismuth Germanate $BiY_{1-x}R_xGeO_5$ Host

C. Cascales* and C. Zaldo*

Instituto de Ciencia de Materiales de Madrid, Consejo Superior de Investigaciones Científicas, C/Sor Juana Inés de la Cruz 3, 28049 Cantoblanco, Madrid, Spain

Received April 4, 2006. Revised Manuscript Received May 29, 2006

The synthesis conditions and structural characteristics of polycrystalline R-doped $BiY_{1-x}R_xGeO_5$ or stoichiometric $BiRGeO_5$ (R = trivalent rare earth Pr^{3+}, Nd^{3+}, Sm^{3+}, Eu^{3+}, Tb^{3+}, Dy^{3+}, Ho^{3+}, Er^{3+}, Tm^{3+}, or Yb^{3+}) germanate compounds are presented. The energy levels of each R^{3+} up to the absorption edge of the germanate matrix have been established from 10 K optical absorption and photoluminescence spectra measurements. Detailed single-electron $C_2(C_s)$ Hamiltonians combining free-ion and crystal-field interactions have been used to model the above $4f^N$ configurations. Very satisfactory correlations were obtained between observed and the calculated energy levels, and corresponding tabulated data are reported. Systematic trends in the evolution of crystal-field parameters have been identified. The proper estimation of phenomenological crystal-field parameters and crystal-field strengths at the R^{3+} site for the whole Pr−Yb series is the first step in prospecting the possibilities of this germanate structure as a new solid-state laser host. The observed medium-high ($\sim$660 cm^{-1}) splitting for the $^2F_{7/2}$ ground state of Yb^{3+} in $BiYbGeO_5$ fulfills a prerequisite for an efficient Yb quasi-three-level laser operation. The possibility of accepting large amounts of optically active R^{3+} ions and the intense Raman shifts observed at high frequencies are other advantageous characteristics of the title host.

I. Introduction

The optical properties of trivalent lanthanide R^{3+} ions embedded in inorganic (single crystal, polycrystalline, or glassy) materials,[1] supramolecular complexes,[2] and polymeric hosts,[3] in several morphologies,[4−6] suppose a continuous focus of research in terms of both their fundamental and technological interest, given that the uses of such materials are steadily increasing, typically as laser and nonlinear optical systems,[7] new magnetic materials,[8] or optoelectronic polymer devices (waveguides[9] and amplifiers[10]).

For the application of a compound as a solid-state laser, the initial evaluation of potentialities of the host,[1c,11−15] as well as the assessment for performance enhancement of already known R^{3+} lasers,[16,17] requires the determination of useful spectroscopic parameters, among which those derived from the crystal-field (CF) analysis of the optical absorption (OA) and photoluminescence (PL) spectra are of substantial importance.[18,19] For instance, in the design of improved R^{3+} quasi-three-level lasers the reduction of the thermal population of the lower level of the laser transition supposes a continuous search for larger CF splitting of the corresponding ground-state manifold,[16,17] and it is particularly important in the context of diode pumping technology for Yb^{3+} lasers now searched as an alternative to Nd^{3+} lasers for the $\lambda \approx 1$ μm emission.[20] On the other hand, the development and study of crystalline hosts accepting a high density of optically active R^{3+} ions, even up to the full R^{3+} stoichiometry, is

* To whom correspondence should be addressed. E-mail: ccascales@icmm.csic.es; cezaldo@icmm.csic.es.

(1) See, for instance, (a) Reisfeld, R.; Ziganski, E.; Gaft, M. *Mol. Phys.* **2004**, *102*, 1319, and recent papers from authors: (b) Cascales, C.; Balda, R.; Fernández, J. *Opt. Express* **2005**, *13*, 2141; (c) Cascales, C.; Zaldo, C.; Sáez Puche, R. *Chem. Mater.* **2005**, *17*, 2052; (d) Cascales, C.; Balda, R.; Fernández, J.; Fdez-Navarro, J. M. *J. Non-Cryst. Solids* **2006**, *352*, 2448.
(2) Torelli, S.; Imbert, D.; Cantuel, M.; Bernardinelli, G.; Delahaye, S.; Hauser, A.; Bünzli, J. C. G.; Piguet, C. *Chem. Eur. J.* **2005**, *11*, 3228, and references therein.
(3) Guo, X.; Zhu, G.; Fang, Q.; Xue, M.; Tian, G.; Sun, J.; Li, X.; Qiu, S. *Inorg. Chem.* **2005**, *44*, 3850.
(4) Yan, R. X.; Li, Y. D. *Adv. Funct. Mater.* **2005**, *15*, 763.
(5) Song, H. W.; Lu, L. X.; Yang, L. M.; Lu, S. Z. *J. Nanosci. Nanotechnol.* **2005**, *5*, 1519.
(6) Le Quang, A. Q.; Zyss, J.; Ledoux, I.; Truong, V. G.; Jurdyc, A. M.; Jacquier, B.; Le, D. H.; Gibaud, A. *Chem. Phys.* **2005**, *318*, 33.
(7) Kaminskii, A. A. *Phys. Status Solidi A* **2003**, *200*, 215.
(8) Doerr, M.; Rotter, M.; Lindbaum, A. *Adv. Phys.* **2005**, *54*, 1.
(9) Kik, P. G.; Polman, A. *MRS Bull.* **1998**, *23*, 48.
(10) Slooff, L. H.; van Blaaderen, A.; Polman, A.; Hebbink, G. A.; Klink, S. I.; Van Veggel, F. C. J. M.; Reinhoudt, D. N.; Hofstraat, J. W. *J. Appl. Phys.* **2002**, *91*, 3955.
(11) Volkov, V.; Cascales, C.; Kling, A.; Zaldo, C. *Chem. Mater.* **2005**, *17*, 291.
(12) Zaldo, C.; Rico, M.; Cascales, C.; Pujol, M. C.; Massons, J.; Aguiló, M.; Díaz, F.; Porcher, P. *J. Phys: Condens. Matter* **2000**, *12*, 8531.
(13) Rico, M.; Volkov, V.; Cascales, C.; Zaldo, E. *Chem. Phys.* **2002**, *279*, 73.
(14) Méndez-Blas, A.; Rico, M.; Volkov, V.; Zaldo, C.; Cascales, C. *Mol. Phys.* **2003**, *101*, 941.
(15) Méndez-Blas, A.; Rico, M.; Volkov, V.; Cascales, C.; Zaldo, C.; Coya, C.; Kling, A.; Alves, L. C. *J. Phys.: Condens. Matter* **2004**, *16*, 2139.
(16) Walsh, B. M.; Barnes, N. P.; Petros, M.; Yu, J.; Singh, U. *J. Appl. Phys.* **2004**, *95*, 3255.
(17) Walsh, B. M.; Grew, G. W.; Barnes, N. *J. Phys.: Condens. Matter* **2005**, *17*, 7643.
(18) Colón, C.; Alonso-Medina, A.; Montero, J.; Fernández, F.; Cascales, C. *J. Chem. Phys.* **2003**, *119*, 13007.
(19) Colón, C.; Alonso Medina, A.; Fernández, F.; Sáez Puche, R.; Volkov, V.; Cascales, C.; Zaldo, C. *Chem. Mater.* **2005**, *17*, 6635.
(20) Haumesser, P. H.; Gaumé, R.; Viana, B.; Antic-Fidancev, E.; Vivien, D. *J. Phys.: Condens. Matter* **2001**, *13*, 5427.

10.1021/cm060785t CCC: $33.50
Published on Web 07/11/2006

encouraged in the thin disk laser technology[21,22] to adequately reduce the thickness of the laser crystal element.

The crystal structure of new germanates $BiYGeO_5$ and $BiYbGeO_5$ grown as single crystals was described with the orthorhombic symmetry of the space group *Pbca* (No. 61).[23] Y^{3+} or Yb^{3+} fully occupy a single site in the structure, with the lowest symmetry C_1. Although single-crystal X-ray analysis showed the existence of some extra Bi atoms (from the Bi_2O_3 used as flux) sharing the position of Y in the first crystal, this partial substitution has not been detected in the Yb crystal. X-ray powder diffraction (XRPD) analysis of samples prepared for all optically active R^{3+} cations indicated that the $BiY_{1-x}R_xGeO_5$ orthorhombic *Pbca* phase can be prepared up to the stoichiometric composition for R = Sm to Yb, i.e., $0 < x \leq 1$, whereas for the larger R cations, Pr and Nd, it can be prepared only for $x \leq 0.35$ compositions.[24] Given that the $4f^6$ configuration of Eu^{3+} is the most suitable CF probe in a new matrix, the authors simulated the CF interactions through corresponding CF parameters for the approximate C_{2v} and then $C_2(C_s)$ symmetries of Eu^{3+} using energy levels derived from measurements of 10 K OA and PL spectra of $BiEuGeO_5$.[24]

In the current work we present the synthesis conditions and the XRPD structure characterization of polycrystalline samples throughout the whole R^{3+} series. The first aim of the present study is to provide experimental data, from low temperature, 10 K, OA and PL spectra measurements, concerning the positions of the energy levels for the entire R^{3+} series, in stoichiometric $BiRGeO_5$, R = Sm^{3+}, (Eu^{3+}), Tb^{3+}, Dy^{3+}, Ho^{3+}, Er^{3+}, Tm^{3+}, and Yb^{3+}, or doped $BiY_{1-x}R_xGeO_5$, R = Pr^{3+} and Nd^{3+}, materials. Detailed single-electron $C_2(C_s)$ Hamiltonians combining together free-ion and CF interactions have been used to simulate the above $4f^N$ energy levels and their associated wave functions in order to get out a phenomenological evaluation of CF parameters. The discussion of observed trends for their variation along the R series will constitute the second point of interest of the work. The confident estimation of the strength of the CF at the R site implies the proper determination of the R^{3+} energy level schemes in this new host, which is one initial step in prospecting possibilities of the structure for solid-state laser technology. The establishment of the sequence of $^2F_{7/2}$ and $^2F_{5/2}$ Stark energy levels in $BiYbGeO_5$ is especially relevant given the current interest on new Yb^{3+} laser matrixes, the alternative to diode-pumped Nd^{3+} ones as before stated. Complementary data on the characterization of the $BiYGeO_5$ host, i.e., its observed transparency UV−NIR range as well as the measurement of the spontaneous Raman shifts for some $BiRGeO_5$ compounds, have also been obtained.

II. Experimental Section

Synthesis and X-ray Diffraction Analysis. Stoichiometric $BiRGeO_5$ or R-doped $BiY_{1-x}R_xGeO_5$ (R = Pr^{3+}, Nd^{3+}, Sm^{3+}, Tb^{3+}, Dy^{3+}, Ho^{3+}, Er^{3+} Tm^{3+}, and Yb^{3+}) polycrystalline samples were prepared in zirconia crucibles, LECO 528-018, by solid-state reaction from mixtures of the stoichiometric required amounts of reagent-grade Bi_2O_3 (99.9%, Strem Chemicals), Y_2O_3 (Research Chemicals, 99.9%), R_2O_3 (99.9%, Cerac Inc.), and GeO_2 (99.999%, ABCR). The mixtures were ground, heated in air at successive temperatures (K) of 1073, 1173, and 1223, quenched, and reground after each of these steps. For identification purposes, the crystal structure and the purity of the expected orthorhombic phase in the products of the above reaction were tested by room-temperature XRPD analyses with a Bruker D-8 diffractometer, using Cu Kα radiation. 2θ scans in the angular range of $5 \leq 2\theta \leq 60$ by 0.02° steps, with a counting time of 2 s each step, were performed and compared with corresponding simulated patterns on the basis of the single-crystal data of previously studied $BiYGeO_5$ and $BiYbGeO_5$.[23] Very small amounts of crystalline $R_2Ge_2O_7$ phases for R = Er,[25] Tm,[26] and Yb[27] compounds have been detected together with the main $BiRGeO_5$ materials, and traces of the cubic $Bi_4(GeO_4)_3$[28] appear for R = Pr, Nd, and Er. Unit cell parameters of stoichiometric Sm to Yb materials as well as of Pr and Nd-doped $BiY_{1-x}R_xGeO_5$ ($x = 0.35$) were determined through Rietveld profile refinements[29] of more accurate XRPD patterns measured in the angular range $5 \leq 2\theta \leq 100$, for 7 s each 0.02° 2θ step.

Optical Spectroscopy Measurements. Optical absorption OA measurements in the above germanate systems were recorded in the range ~4000−30000 cm^{-1} with a Varian 5E spectrophotometer. Continuous wave photoluminescence (PL) spectra were obtained by pumping with several lasers, namely, a Coherent 7W Ar^+ single line laser, a Spectra Physics Ti-sapphire laser, and an Exciton DUO dye laser system. The emission was analyzed with a Spex 340E spectrometer (f = 34 cm) and detected with a cooled R928 Hamamatsu photomultiplier (185−900 nm), a 77 K cooled Ge photodiode [model ADC-403 IR (1.0−1.7 μm)], or a 77 K cooled InSb photovoltaic detector [model Hamamatsu P5968-060 (1.1−5.5 μm)]. The signal detector was recorded by using a lock-in amplifier. The samples, consisting of dispersed $BiRGeO_5$ or $BiY_{1-x}R_xGeO_5$ powders in KBr pellets, were cooled to 10 K using a He close cycled cryostat connected to a suitable temperature controller. Room-temperature IR spectra were acquired in a Bruker ISS 66V-S spectrophotometer, with samples dispersed in KBr. Room-temperature Raman spectra were obtained with a Reninshaw Ramascope 2000 equipped with a CCD detector, and the polycrystalline samples were excited with the 514.5 nm line of an Ar^+ laser. The spectra were recorded in the backscattering geometry at room temperature and corrected by the spectral response of the experimental setup.

III. Structural Background and Optical Characterization

Pale-colored $BiRGeO_5$ or $BiY_{1-x}R_xGeO_5$ compounds present a crystalline phase isostructural with the centrosymmetric orthorhombic *Pbca* structure type established for $BiYGeO_5$ and $BiYbGeO_5$.[23] The structure, see Figure 1, is constituted by *ac* $[GeRO_5]_\infty$ layers containing both $(RO_7)_6$

(21) Giesen, A.; Hugel, H.; Voss, A.; Wittig, K.; Brauch, U.; Opower, H. *Appl. Phys., B* **1994**, *58*, 365.
(22) Contag, K.; Karszewski, M.; Stewen, C.; Giesen, A.; Hugel, H. *Quantum Electron.* **1999**, *29*, 697.
(23) Cascales, C.; Campá, J. A.; Gutiérrez Puebla, E.; Monge, M. A.; Ruíz Valero, C.; Rasines, I. *J. Mater. Chem.* **2002**, *12*, 3625.
(24) Cascales, C.; Zaldo, C. *J. Solid State Chem.* **2003**, *171*, 262.
(25) PDF # 38-0290, PCPDFWin of JCPDS-International Centre for Diffraction Data, 2001.
(26) PDF # 47-0296, PCPDFWin of JCPDS-International Centre for Diffraction Data, 2001.
(27) PDF # 45-0531, PCPDFWin of JCPDS-International Centre for Diffraction Data, 2001.
(28) PDF # 34-0416, PCPDFWin of JCPDS-International Centre for Diffraction Data, 2001.
(29) Roisnel, T.; Rodriguez-Carvajal, J. WinPLOTR 2003, http://www-llb.cea.fr/fullweb/winplotr/winplotr.htm.

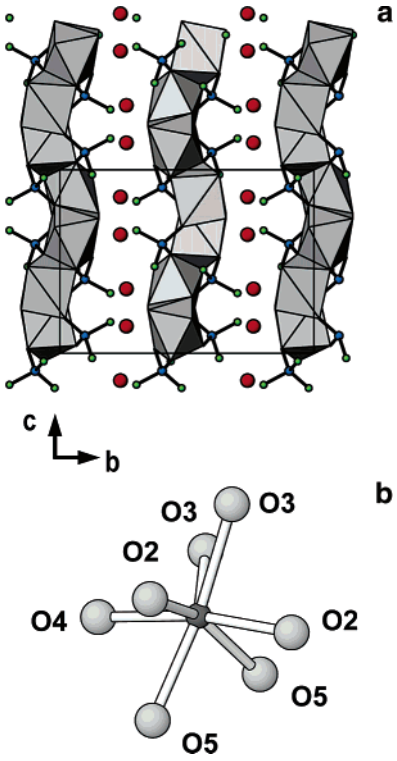

Figure 1. Top: View along the [100] direction of the $BiRGeO_5$ structure showing edge-sharing RO_7 polyhedra in the *ac* $[GeRO_5]_\infty$ layers. Small spheres in tetrahedral coordination correspond to GeO_4 groups and large spheres represent Bi atoms. Bottom: RO_7 monocapped trigonal prism coordination polyhedron: its symmetry can be taken, in a first approach, as C_{2v}.

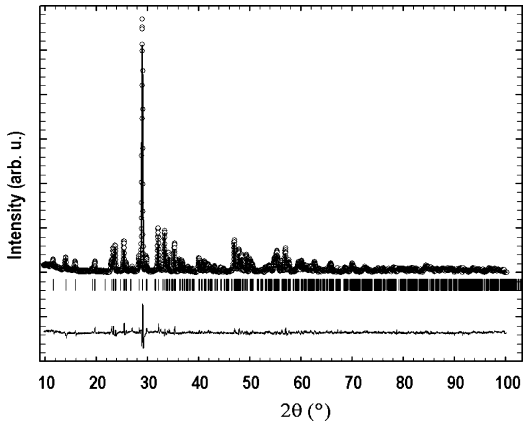

Figure 2. Observed XRPD pattern of $BiTbGeO_5$ (circles). The solid line is the calculated profile and the vertical marks correspond to the position of the Bragg reflections. The difference between the experimental and calculated profiles is plotted at the bottom.

units of edge-sharing RO_7 polyhedra, described as approximate C_{2v} monocapped trigonal prisms, and GeO_4 tetrahedra. R occupies a single-point site in the host, whose real symmetry is C_1. Zigzag chains of ψ-BiO_5 octahedra are running between these layers, in the *a* direction. The stereoelectronic effect of the Bi^{3+} lone pair guides this apparent zigzag, and therefore the kind of packing in this new structure type.

As an example to illustrate the XRPD characteristics of the title materials, Figure 2 shows the Rietveld refinement profile of the pure and well-crystallized $BiTbGeO_5$ compound. Table 1 includes the determined unit-cell parameters of stoichiometric $BiRGeO_5$, R = Sm−Yb, and R-doped

Table 1. Unit Cell Parameters of $BiRGeO_5$ and Pr or Nd-Doped $BiY_{1-x}R_xGeO_5$ Compounds

	a/Å	*b*/Å	*c*/Å	*V*/Å^3
$Y_{0.65}Pr_{0.35}$	5.3623(4)	15.223(1)	11.137(1)	909.1(1)
$Y_{0.65}Nd_{0.35}$	5.3642(4)	15.223(1)	11.1426(9)	909.9(1)
Y[a]	5.341(8)	15.232(2)	11.084(3)	901.9(3)
Sm	5.4125(8)	15.283(2)	11.275(2)	932.7(3)
Eu	5.3952(4)	15.262(1)	11.2263(9)	924.4(1)
Tb	5.3650(4)	15.241(1)	11.1422(9)	911.1(1)
Dy	5.3455(4)	15.212(1)	11.0855(8)	901.4(1)
Ho	5.3267(3)	15.1865(9)	11.0337(7)	892.58(9)
Er	5.3230(8)	15.212(1)	11.017(2)	892.1(2)
Tm	5.2993(4)	15.180(1)	10.9680(9)	882.3(1)
Yb	5.2885(3)	15.166(8)	10.9354(6)	877.08(8)

[a] From ref 23. Single-crystal data.

$BiY_{1-x}R_xGeO_5$, $x = 0.35$, R = Pr and Nd, compounds that show nearly linear expansions with increasing R ionic radius.

The inert $BiYGeO_5$ host is transparent in the UV-near-IR spectral range from 300 to 3600 nm (0.30−3.8 μm). Room-temperature Raman spectra show intense frequency shifts peaking at 58(58), 65(64), 151(151), 175(174), 208(206), 365(365), 515(514), 799(797), 1046(1048), 1058(1058), 1089(1090), 1104(1103), 1150(1151), 1178(1178), 1496-(1495), and 1544(1543) cm^{-1} for $BiYGeO_5$($BiYbGeO_5$), being these which appear at higher frequencies very strong for the Yb compound.

IV. Low-Temperature Optical Absorption and Photoluminescence Spectra

Summary of Experimental R^{3+} Energy Levels. The $^{2S+1}L_J$ states of the $4f^N$ R^{3+} configurations in this germanate matrix are split in the maximum number of Stark components, $2J + 1$ singlets for N = even or $J + {}^1/_2$ Kramers doublets for N = odd. In that follows details on the assignment of the energy levels are indicated.

Excepting for Eu^{3+}, all experimental data tabulated have been drawn from measurements made in the course of the present work. Anyway, for $BiEuGeO_5$ calculated energy levels and derived CF parameters have been re-evaluated and therefore they are also currently appearing. Earlier experimental and CF analysis details can be seen elsewhere.[24]

Pr^{3+} in $BiY_{0.65}Pr_{0.35}GeO_5$. Well-resolved transitions in the OA spectrum of Pr^{3+} at 10 K originate mainly from the lowest Stark component $^3H_4(0)$ of the ground-state manifold. At this temperature only one intense band corresponding to the transition from $^3H_4(0)$ to $^3P_0$ is detected, confirming the existence of only one crystallographic point site for Pr^{3+}. The contribution arising from the thermally populated first excited level $^3H_4(1)$ appears as a lesser intense transition situated at the low-energy side, at 23 cm^{-1}, of the former band. Transitions from $^3H_4(0)$ to the $^1I_6$ state appear, as expected, with very low intensity, and only one $^1I_6$ energy level has been assigned, which anyway is not distinguishable from possible vibronic structure associated with the more intense $^3P_1$ levels. The sequence of energy levels for $^3F_{2,3,4}$, $^1D_2$, and $^3P_{0,1,2}$ has been established from the OA spectrum. The energy positions of the Stark levels of $^3H_5$ have been deduced from the PL emissions corresponding to the 10 K de-excitation of the low component of the $^1D_2$, while the positions of the $^3H_6$ energy levels were determined from the

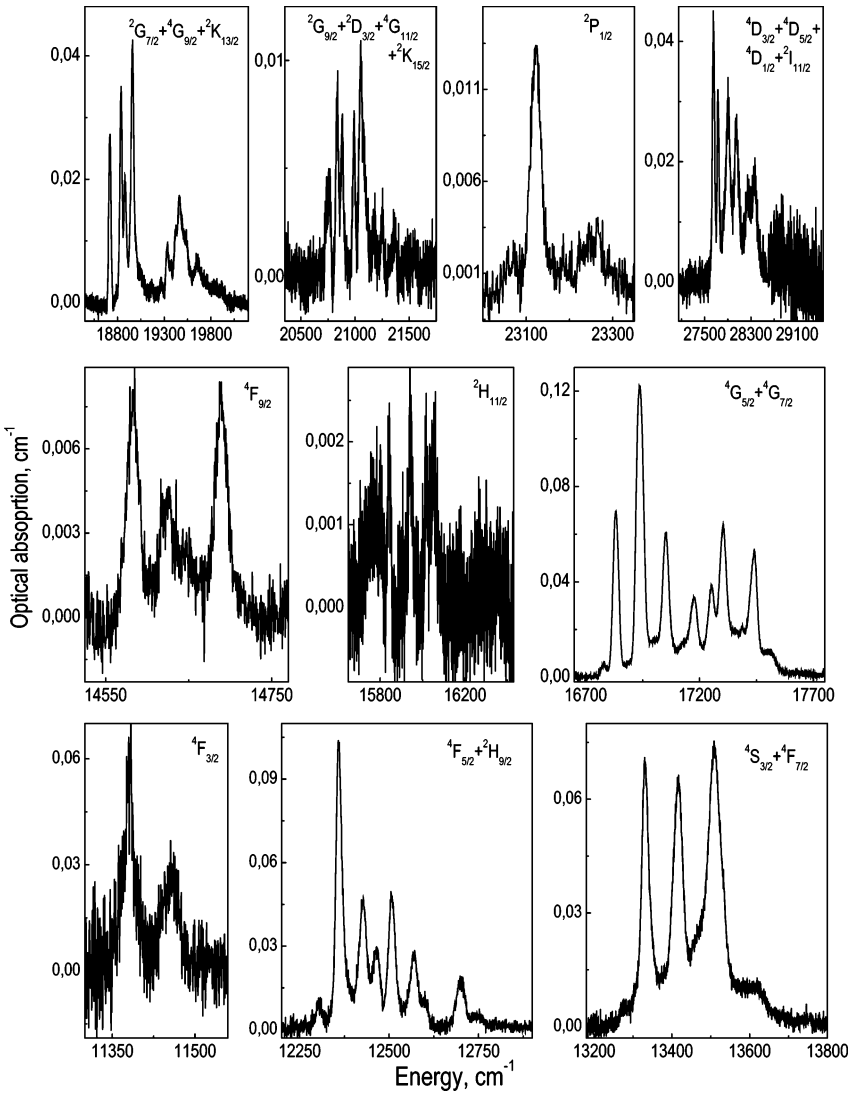

Figure 3. 10 K optical absorption spectra of Nd^{3+} in $BiY_{0.65}Nd_{0.35}GeO_5$.

PL of the $^3P_0$ singlet, from which the sequence of levels for $^3F_2$ can be further assessed. The energies of the $^3H_4$ multiplet have been determined from the thermal behavior of transitions $^3H_4 \rightarrow {}^3P_0$. These experimental results are not shown for the sake of brevity. In summary, 34 energy levels were experimentally established, see Table A1 of the Supporting Information, and with the exception of the $^1D_2$ ones, used in the subsequent crystal-field analysis.

Nd^{3+} in $BiY_{0.65}Nd_{0.35}GeO_5$. The 10 K OA spectra corresponding to electronic transitions of Nd^{3+} show well-resolved and intense bands at ~560−600, 720−760, and 790−820 nm. They have their origin in the first Stark level of the $^4I_{9/2}$ ground multiplet, and the unique band corresponding to the $^4I_{9/2} \rightarrow {}^2P_{1/2}$ transition reveals the existence of only one Nd^{3+} active center. From these spectra the energy positions of levels from $^4F_{3/2}$ up to $^4D_{1/2}$ have been derived. As Nd^{3+} is a laser ion often taken for reference, Figure 3 gives an overview of these 10 K OA spectra.

Energy level positions of the ground $^4I_{9/2}$, and excited $^4I_{11/2}$ and $^4I_{13/2}$ multiplets have been established from PL measurements from the lowest level of $^4F_{3/2}$, as shown for reference in Figure 4. Lesser intensity emission bands arising from the $^4F_{3/2}$ high-energy component, 75 cm^{-1} above, Figure 3, unambiguously reproduce the sequence of these $^4I_{9/2}$ and $^4I_{11/2}$ and $^4I_{13/2}$ crystal-field levels.

In summary, the 65 energy levels collected in Table A2 of the Supporting Information have been established from OA and PL spectra and used in the subsequent crystal-field analysis.

Sm^{3+} in $BiSmGeO_5$. One hundred ninety-eight SLJ manifolds, which can split into a total of 1001 energy levels, characterize the $4f^5$ configuration of Sm^{3+}; thus, its energy level scheme is one of the most complicated among all R^{3+} ions. However, the $^{2S+1}L_J$ levels form rather isolated groups up to ca. 25000 cm^{-1}, beyond which the density of energy levels becomes almost inaccessible. The 10 K OA spectra of the pure stoichiometric samarium germanate were measured between ~2000 and 350 nm corresponding to transitions from the lowest energy Stark component of the ground-state $^6H_{5/2}$ to excited levels above 4900 cm^{-1}, i.e., from $^6H_{13/2}$ to $^2H1_{7/2}$ energy levels. Figure 5 displays the observed 10 K OA transitions along with their assignments.

In the NIR region between the observed $^6H_{13/2}$ and $^6F_{11/2}$ states the unambiguous assignment of the crystal-field levels is only hampered by the overlap of $^6H_{15/2}$ and $^6F_{1/2-3/2}$ multiplets. Transitions to other $^6F_{5/2-11/2}$ states are well-

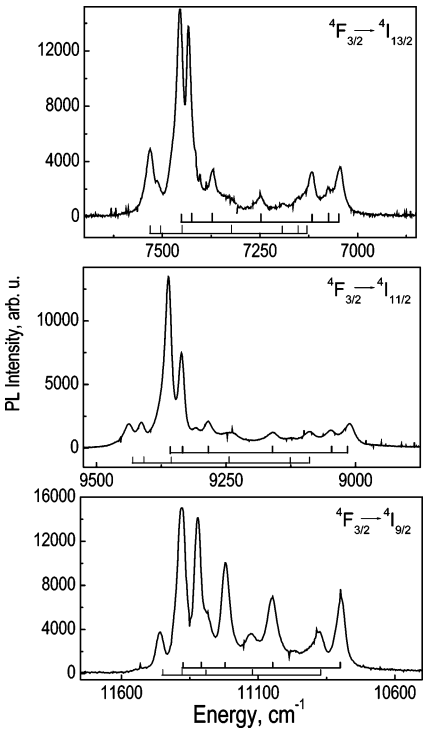

Figure 4. 10 K photoluminescence spectra of Nd^{3+} in $BiY_{0.65}Nd_{0.35}GeO_5$. $\lambda_{EXC} = 514$ nm (Ar^+ laser).

resolved. In the visible and UV regions below 505 nm the density of the absorption lines increases, as shown in Figure 5, and the *J* mixing of states becomes high. In consequence the final assignment of levels will be decided by the crystal-field analysis of these spectra.

A nearly complete sequence for the ground $^6H_{5/2}$ and excited $^6H_{7/2-11/2}$ energy levels has been established from PL measurements from the lowest level of $^4G_{5/2}$.

The collection of 111 Sm^{3+} observed energy levels given in Table A3 of the Supporting Information have been established from OA and PL spectra and used in the subsequent crystal-field analysis.

Eu^{3+} in $BiEuGeO_5$. The experimental determination of Eu^{3+} energy levels has been conducted in a previous work, [24] and these results are now used as the starting point for the current CF analysis. It is well-known that Eu^{3+} is the best choice for a "crystal-field probe" in a given host. Their ground $^7F_0$ as well as the fluorescent $^5D_0$ states are nondegenerate and have the same irreducible representation. This fact largely simplifies the interpretation of the spectra and makes it possible to discriminate between different point symmetries for the observed optical center, especially when polarized measurements are available.[30] Moreover, there is a straightforward relation between the CF splitting of $^{2S+1}L_J$ levels with small *J* values, especially for $J = 1$ and 2, and the CF parameters. In this case, CF parameters can be deduced directly from the experiment. The phenomenological CF modeling of the Eu^{3+} energy level scheme, which can be realistically conducted on the strongly reduced basis of the $^7F_{JM}$ set alone, i.e., 49 $|SLJM_J\rangle$ levels,[24] has been reconsidered in light of the information provided by neighboring R^{3+} ions. The calculated energy levels and a new set of derived CF parameters appear in Table A4 of the Supporting Information, along with the 29 Eu^{3+} energy levels observed earlier.[24]

Tb^{3+} in $BiTbGeO_5$. With 3003 crystal-field levels, the $4f^8$ configuration of Tb^{3+} is overcome in complexity only by that of the $4f^7$ of Gd^{3+}. As in the case of Eu^{3+}, this problem can be handled by realizing the large energy gap between the ^7F_J ground levels and the $^5D_4$ and $^5D_3$ emitting levels (14000 and 20000 cm^{-1}, respectively), as well as the difference in spin and orbital multiplicities between them. Accordingly, the interactions between the ground multiplet and the rest of the configuration will be of minor importance; that is, the wave functions are weakly mixed in accordance with the free-ion selection rules. On the other hand, when compared to Eu^{3+} in the same host, the interpretation and assignment of both their OA and PL spectra are complicated by the high *J* degeneracy of the $^7F_6$ ground multiplet as well as by the two possible emitting levels $^5D_4$ and $^5D_3$, and in fact, crystal-field analysis conducted on Tb^{3+} has been much more scarce than those on Eu^{3+}.[30]

Figure 6 shows the 10 K PL spectra of Tb^{3+} in the germanate host. At this temperature the Tb^{3+} PL occurs from the lowest crystal-field level of the excited $^5D_4$ state. All the $^5D_4$ to $^7F_{0-6}$ transitions are in the visible range, and are relatively strong, in contrast to the ^5D_J to $^7F_{5-6}$ previously seen for Eu^{3+}, which are weak and appeared in the IR region. More information about the ^7F_J septuplet is thus obtained from Tb^{3+} than from Eu^{3+}, and the total absence of overlapping transitions allows the different $^5D_4 \rightarrow {}^7F_J$ to be easily identified. In this way, 39 CF energy levels, collected in Table A5 in the Supporting Information, have been determined and then used in the modeling of CF effects.

Dy^{3+} in $BiDyGeO_5$. The bands observed in the 10 K OA spectra of $BiDyGeO_5$ are due to transitions from the lowest energy level of the $^6H_{15/2}$ ground multiplet to the excited Stark energy levels $^6H_{11/2}$ and beyond in the $4f^9$ Dy^{3+} configuration. Although not shown for the sake of brevity, well-resolved transitions up to 325 nm ($\sim$30730 cm^{-1}, $^6P_{3/2}$) have been collected.

In the NIR region, the first state observed was $^6H_{11/2}$, for which all six energy levels were resolved. Also, the regions between 1220 and 1300 and from 1050 to 1110 are well-resolved, yielding almost complete Stark energy level sequences for the corresponding transitions to $^6H_{9/2} + {}^6F_{11/2}$ as well as to $^6H_{7/2} + {}^6F_{9/2}$, although in both sets a partial overlap is found. The intensities of the transitions $^6H_{15/2} \rightarrow {}^6F_{7/2}$ ($\sim$890−905 nm) and $^6H_{15/2} \rightarrow {}^6H_{5/2}$ ($\sim$960−990 nm) are weak and very weak, respectively, and $^6H_{15/2} \rightarrow {}^6F_{1/2}$ ($\sim$725 nm) is not observed at all. In fact, although sometimes observed through a partial lift by the crystal-field effect, the later transition is forbidden due to the $\Delta J \leq 6$ free-ion selection rule. Beyond 400 nm the density and wave function mixing of SLJ states becomes more important, resulting in severe overlap of these states. The assignment of transitions to specific energy levels has been made through the performed CF analysis.

(30) Görller-Walrand, C.; Binnemans, K. Rationalization of Crystal-Field Parametrization. In *Handbook on the Physics and Chemistry of Rare Earths*; Gschneidner, K. A., Jr., Eyring, L., Eds., Elsevier Science: Amsterdam, 1995; Vol. 23; p 121.

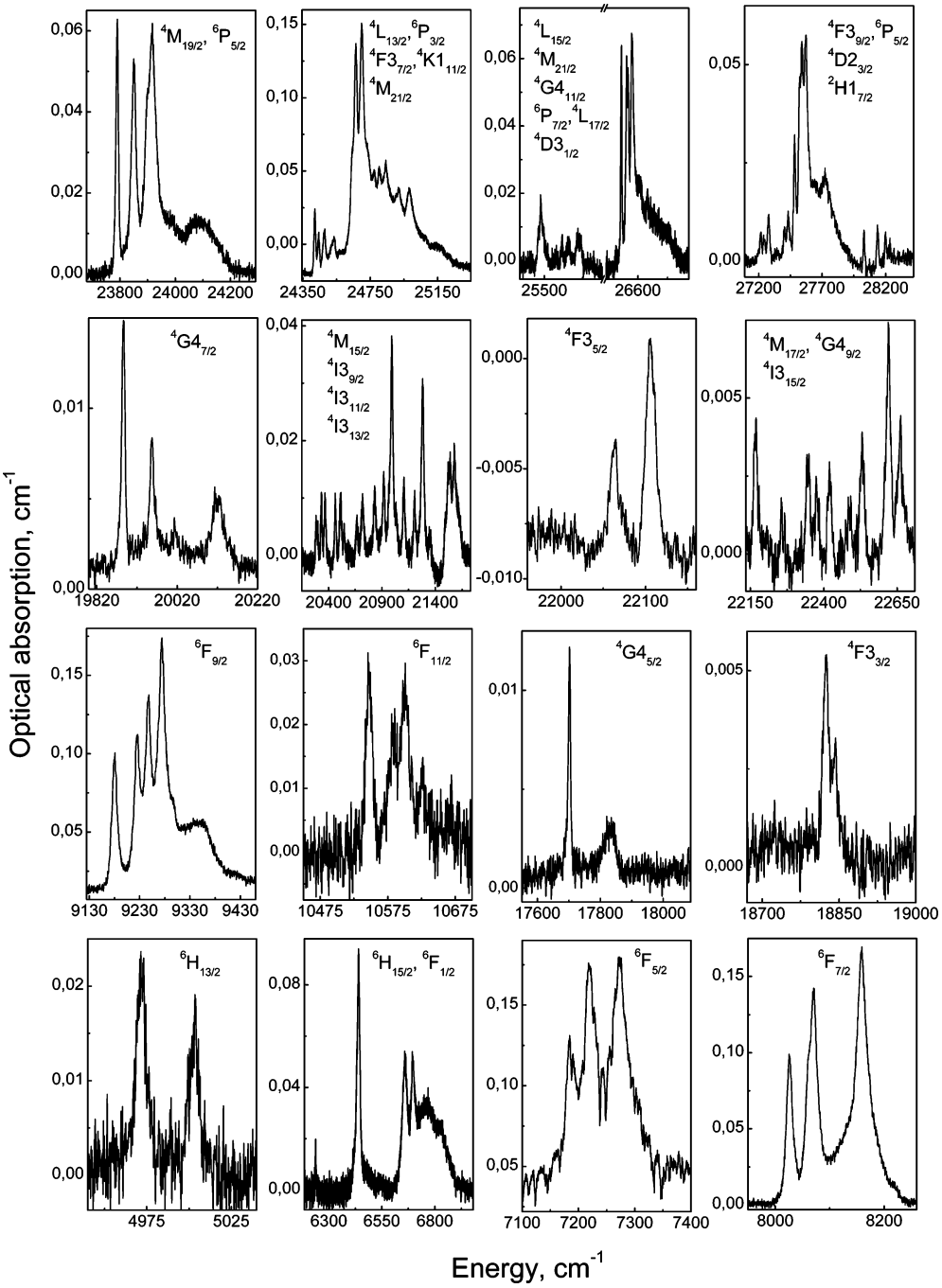

Figure 5. 10 K optical absorption spectra of Sm^{3+} in $BiSmGeO_5$.

To determine the lowest excited Starks levels of the ground $^6H_{15/2}$ multiplet, OA spectra at selected temperatures between 10 and 300 K were measured. Moreover, the seven $^6H_{13/2}$ Stark levels of Dy^{3+} have been determined from 10 K PL emissions originating from the $^4F_{9/2}$ state de-excitation. For this purpose a $BiY_{0.65}Dy_{0.35}GeO_5$ sample was used.

The 89 energy levels included in Table A6 of the Supporting Information have been derived from the above measurements, and they have been used in the current simulation of CF interactions.

Ho^{3+} in $BiHoGeO_5$. Assignments of energy levels of the $4f^{10}$ configuration of Ho^{3+} are usually complicated by the existence, even at very low temperatures, of satellite bands, which arise from the thermal population of the first and even second excited energy levels, located some cm^{-1} above $^5I_8$-(0) in the ground-state manifold. The 10 K OA spectra of Ho^{3+} in $BiHoGeO_5$ extend from ~1980 to 360 nm, allowing determination of the energy levels from $^5I_7$ (partially) up to $^3H_4$ multiplets. These OA spectra apparently do not contain transitions from excited $^5I_8$ Stark levels. Bands corresponding to $^5I_8 \rightarrow {}^5I_6$ transitions appear with very low intensity, and those corresponding to $^5I_8 \rightarrow {}^5I_5$ and $^5I_8 \rightarrow {}^5I_4$ transitions have not been observed.

Observed 10 K PL emissions to the ground $^5I_8$ multiplet originate from the $^5F_5$ state, and the Stark level structure of $^5I_7$ has been established from PL spectra associated with emission transitions from $^5S_2$. Furthermore, assignments of $^5I_8$ energy levels have been confirmed through transitions from $^5I_7$. Taking into account that the first excited level is resolved at 63 cm^{-1} above $^5I_8(0)$, it is not surprising the lack

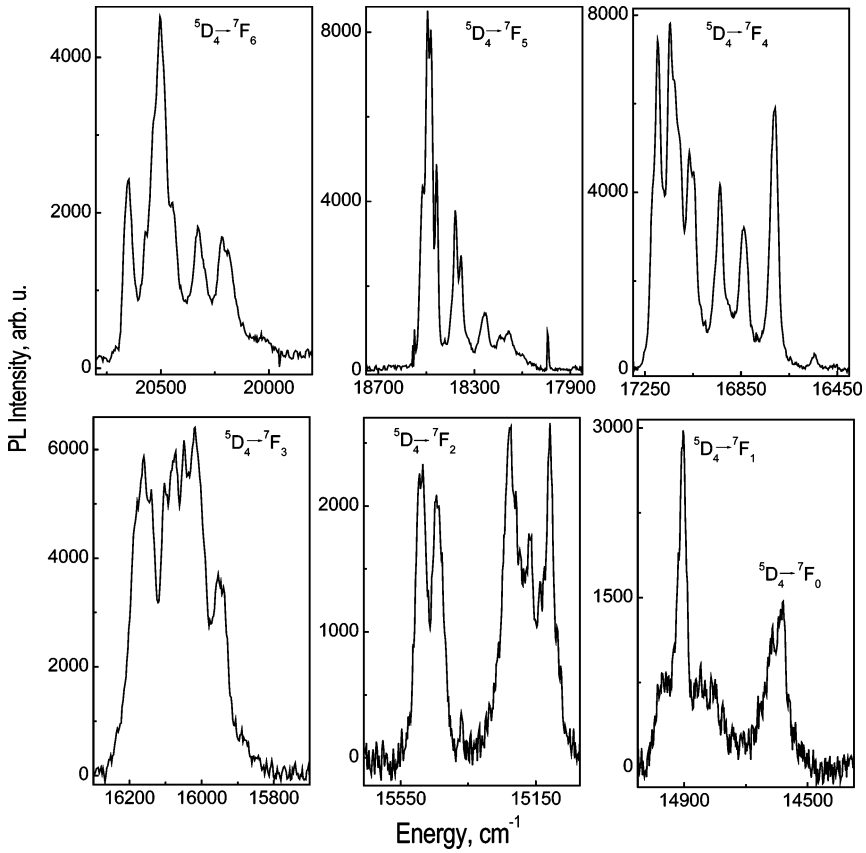

Figure 6. 10 K photoluminescence spectra of Tb^{3+} in $BiTbGeO_5$. Multiline (λ_{EXC} = 334, 351, 363 nm) ultraviolet Ar^+ laser.

of the usual hot bands accompanying most of the transitions.

Table A7 of the Supporting Information includes the 101 energy levels experimentally observed and then used in the parametrization of CF effects.

Er^{3+} in $BiY_{1-x}Er_xGeO_5$, $x = 0.05-1.0$. The OA measurements of the polycrystalline sample prepared with the nominal Er stoichiometric $BiErGeO_5$ composition showed the coexistence of several Er^{3+} centers. The OA bands of lesser intensity were identified as corresponding to $Er_2Ge_2O_7$,[31] present in the sample as a secondary phase. The relative intensity of the bands associated with this later phase decreases with decreasing Er concentrations in the $BiY_{1-x}Er_xGeO_5$ samples. Therefore, the comparative study of the 10 K spectroscopy of the $4f^{11}$ configuration of Er^{3+} carried out for $x = 0.05$, 0.20, 0.35, and 1.0 allows identification of the bands associated with the $BiY_{1-x}Er_xGeO_5$ phase. From 10 K OA measurements between ~1540 and 356 nm of the $x = 0.2$ sample, the energy levels of multiplets from $^4I_{13/2}$ up to $^4G_{7/2}$ have been derived. At 10 K the OA transitions with the origin in $^4I_{15/2}(0)$ were relatively isolated and appeared well-resolved, even the weaker ones, namely, to $^4I_{11/2}$ (10200−10400 cm^{-1}), $^4F_{7/2}$ (20400−20650 cm^{-1}), and $^4F_{3/2}$ (22500−22600 cm^{-1}). However, the thermal effect arising from the population of the first excited level of the $^4I_{15/2}$ ground multiplet is not completely absent at 10 K, and the energy of this $^4I_{15/2}(1)$ Stark level can be determined from the weak band seen displaced 16 cm^{-1} at the low-energy side of nearly all OA transitions through the whole spectra.

The energies of the Stark levels of the $^4I_{15/2}$ ground multiplet have been derived from 10 K PL measurements of the $^4I_{13/2} \rightarrow {}^4I_{15/2}$ transition carried out in the four prepared *x*-composition samples, which yielded identical results in all cases. Furthermore, the study of the 10 K PL for the $^4S_{3/2} \rightarrow {}^4I_{13/2}$ transition in the $BiY_{0.65}Er_{0.35}GeO_5$ sample corroborates the sequence of energy levels for $^4I_{13/2}$ established as derived of the 10 K OA spectrum measurements.

Table A8 of the Supporting Information includes the set of 66 energy levels determined from OA and PL measurements.

Tm^{3+} in $BiY_{1-x}Tm_xGeO_5$, $x = 0.35$, 1.0. As in the previous erbium case, the coexistence of a minoritary $Tm_2Ge_2O_7$ phase was observed by XRPD analyses of the sample with nominal $BiTmGeO_5$ composition. To separate the contribution arising from this minoritary phase from that corresponding to Tm^{3+} embedded in the current germanate host, measurements with a lesser concentrated sample, $x = 0.35$, were carried out. In this later case, only one Tm^{3+} optical center was observed, allowing the identification of the extra bands in samples with $x = 1$ as transitions corresponding to $Tm_2Ge_2O_7$, which moreover agree with the corresponding energy levels previously indicated for $Tm_2Ge_2O_7$.[31]

At 10 K the OA occurs mainly from the lowest energy level of the $^3H_6$ ground-state multiplet to the excited $^3F_4$, $^3H_5$,$^3H_4$,$^3F_3$,$^3F_2$,$^1G_4$, and $^1D_2$ multiplets, which are well-isolated. The 10 K PL spectrum of $BiY_{0.65}Tm_{0.35}GeO_5$ was excited at λ_{EXC} = 768.8 nm (~13000 cm^{-1}). Under these excitation conditions, the $^3F_4$ state is populated by a cross-

(31) Ghosh, M.; Jana, S.; Ghosh, D.; Wanklin, B. M. *Solid State Commun.* **1998**, *107*, 113.

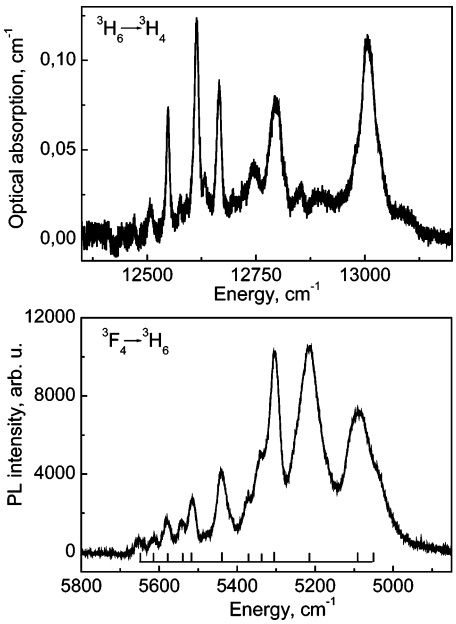

Figure 7. 10 K optical absorption spectrum (top) and $\lambda \approx 2$ μm 10 K photoluminescence spectrum (bottom) of Tm^{3+} in $BiY_{0.65}Tm_{0.35}GeO_5$.

relaxation process from the $^3H_4$ excited multiplet. The observed features are then assigned to the $^3F_4 \rightarrow {}^3H_6$ transition. The same measurements were carried out with the stoichiometric $BiTmGeO_5$ sample, using $\lambda_{EXC} = 795$, 791.8, 777.6, and 768.8 nm, and the spectra yielded identical structure for the $^3H_6$ ground multiplet. This $\lambda \approx 2$ μm PL emission is recently receiving considerable attention for medical applications[32] and as a pump source of high-power ns mid-IR OPOs based on $ZnGeP_2$,[33] and for environmental gas pollution control,[34] all in connection with the diode pumping technology as an alternative to Ho^{3+}. Therefore, in Figure 7 this IR PL spectrum along with the OA spectrum of interest for diode pumping are displayed for reference. The collection of 52 observed energy levels is included in Table A9 of the Supporting Information.

Yb^{3+} in $BiY_{1-x}Yb_xGeO_5$, $x = 0.20$, 1.0. 10 K OA measurements carried out with $BiY_{0.8}Yb_{0.20}GeO_5$ and $BiYbGeO_5$ samples did not allow observation of transitions from the ground $^2F_{7/2}$ multiplet to the excited $^2F_{5/2}$ one. The energy levels of $^2F_{7/2}$ and $^2F_{5/2}$ multiplets were obtained from 10 K emission and excitation PL measurements. The excitation spectra of the Yb stoichiometric sample collected for $\lambda_{EMI} = 1004-1020$ nm provided the $^2F_{5/2}$ Stark levels while the emission spectra displayed those of $^2F_{7/2}$. The $^2F_{5/2}(0') \rightarrow {}^2F_{7/2}$ (n) transition is presently the focus of intense research as an alternative for Nd^{3+} lasers pumped by diode laser emission.[35] Figure 8 shows for reference the 10 K excitation and emission PL spectra, from which the seven Yb^{3+} Stark levels, indicated in Table A10 of the Supporting Information, can be derived.

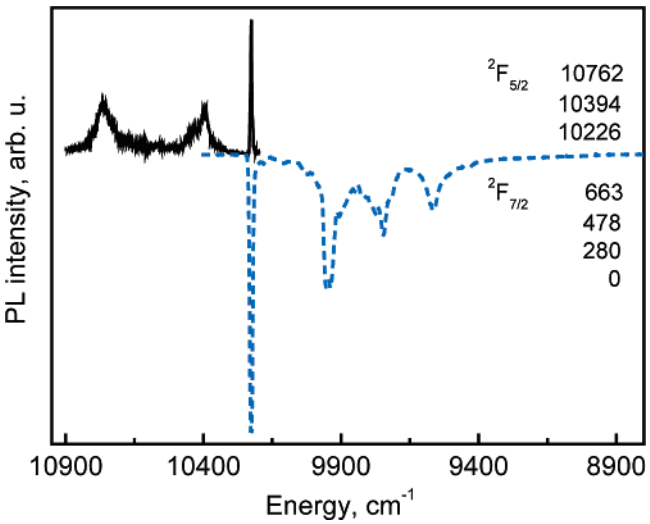

Figure 8. 10 K photoluminescence spectrum of Yb^{3+} in $BiY_{0.8}Yb_{0.2}GeO_5$. The continuous line represents the excitation spectrum taken for $\lambda_{EMI} = 1004$ nm. The dashed line shows inverted the emission spectrum excited at $\lambda_{EXC} = 932$ nm (Ti-sapphire laser).

V. Crystal-Field Modeling and Simulation of the Energy Level Schemes

The effect of the different interactions responsible for the energy levels structure, intraionic H_{FI} as well as CF effects arising from the influence of the surrounding charges on the $4f^N$ electrons, can be described with a combined Hamiltonian $H_T = H_{FI} + H_{CF}$, which includes one or several parameters for each interaction[36]

$$H_T = H_0 + \sum_{k=0,1,2,3} E^k e_k + \zeta_{4f} A_{SO} + \alpha L(L+1) + \beta G(G_2) + \gamma G(R_7) + \sum_{k=0,2,4} M^k m_k + \sum_{i=2,4,6} P^i p_i + \sum_{\lambda=2,3,4,6,7,8} T^\lambda t_\lambda + \sum_{k,q,i} B_q^k C_q^k(i)$$

In the H_{FI} free-ion part of this expression H_0 stands for the spherically symmetric one-electron term of the Hamiltonian. E^k and ζ_{4f} are the Racah parameters and the spin−orbit coupling constant and e_k and A_{SO} represent the angular part of the electrostatic repulsion and spin−orbit coupling, respectively. For the configurations of two or more equivalent electrons the two-body interactions are considered with the Trees parameters α, β, and γ, associated with Casimir operators $G(G_2)$ and $G(R_7)$, and for configurations having more than two electrons, non-negligible three-body interactions must also be accounted through Judd parameters T^λ. Magnetically correlated corrections such as spin−spin and spin−other−orbit interactions can be simulated through the M^k parameters, also called Marvin integrals. Finally, the electrostatically correlated spin−orbit interactions are described by the P^i integrals.

In the one-electron CF part of the total Hamiltonian, C_q^k are related to the spherical tensors of rank k, dependent on the coordinates of the ith electron with summation over all

(32) Fried, N. M. *Lasers Surg. Med.* **2005**, *36*, 52.
(33) Budni, P. A.; Pomeranz, L. A.; Lemons, M. L.; Miller, C. A.; Mosto, J. R.; Chicklis, E. P. *J. Opt. Soc. Am. B* **2000**, *17*, 723.
(34) Mihalcea, R. M.; Webber, M. E.; Baer, D. S.; Hanson, R. K.; Feller, G. S.; Chapman, W. B. *Appl. Phys. B* **1998**, *67*, 283.
(35) Krupke, W. F. *IEEE J. Sel. Top. Quantum Electron.* **2000**, *6*, 1287.
(36) Wybourne, B. G. *Spectroscopic Properties of Rare Earths*; Wiley: New York, 1965.

4f electrons, and B_q^k are the CF parameters, whose k and q values are constrained by the symmetry of the center site.

The current local R^{3+} C_1 site symmetry involves 27 CF parameters, but the simulation with such a high number of adjustable parameters is nonrealistic. Therefore, we proceeded by using the approximate C_2/C_s symmetry as the best approach to the true symmetry of R^{3+} in the $BiRGeO_5$ host. To make a meaningful simulation, we carry out the descending symmetry procedure fitting first the observed energy levels in the orthorhombic C_{2v} point group, the highest symmetry for which no CF degeneracy exists. In the search for reliable minima, the relative accuracy of the starting parameters together with the correctness of the level assignments are crucial requirements. Rough values of the nine C_{2v} CF parameters to be used as starting parameters have been derived from two approaches: (a) in the first we have applied the *Simple Overlap Model* (SOM),[37] a simplified *semiempirical* calculation of CF interactions, to obtain the initial set of CF parameters for Pr^{3+} ($4f^2$) and Tm^{3+} ($4f^{12}$) configurations from the crystallographic structure, as a kind of evaluation of the CF evolution (order of magnitude and signs) along the R^{3+} series, and (b) the consideration of phenomenological sets of C_{2v} and then C_2/C_s CF parameters previously reported for Eu^{3+} [24] is the other, and also the best, possibility. Thus, from Eu^{3+} data, corrected following the observed trends in the SOM results, we began with modeling the observed spectra of Nd^{3+} ($4f^3$) and Er^{3+} ($4f^{11}$) configurations, which afterward were used as models for interpreting the spectra of adjacent ions in the left and right sides of the $4f^N$ series, respectively. Since CF parameters are supposed to exhibit moderate variations over the series,[38] the parameters for one configuration can serve as a reasonable approach of those for a nearest neighbor one. Free-ion FI parameters do not vary much for a lanthanide ion in different systems, and consequently those initially used can be taken from the literature.[38]

The procedure for the simulation of the energy level schemes has supposed the simultaneous treatment of both FI and CF effects, avoiding the arbitrary adjustment of the barycenter of multiplets. For Pr^{3+}, Nd^{3+}, Dy^{3+}, Er^{3+}, Tm^{3+}, and Yb^{3+} configurations the corresponding entire basis sets of wave functions have been diagonalized, while for Sm^{3+} and Ho^{3+} the simulations have considered truncatures from $^2L_{17/2}$ ($\sim$45850 cm^{-1}) and $^1H_{15}$ ($\sim$49600 cm^{-1}), respectively. For Eu^{3+}, and for Tb^{3+} only the ^7F terms have been used in modeling CF effects. Moreover, the previously reported Eu CF interactions[24] have been revised in light of current results for this R^{3+} series.

A true adjustment is not possible for Yb^{3+}. To simulate the experimental $^7F_{5/2}$ and $^7F_{7/2}$ manifolds, we examine the energy level sequences resulting in changes in CF parameters obtained for Er^{3+} and Tm^{3+} (the five complex S_q^k are kept as in $BiErGeO_5$) with small variations in the only two required FI parameters, E^0 and ζ. The set of CF parameters that better reproduce the experimental sequence appears in Table 2.

As a useful tool to measure the CF interaction strength across the $BiRGeO_5$ family, mainly in order to establish quantitative comparisons with other hosts (where possible differences in the symmetry of the R^{3+} site leads to CF potentials described through different sets of CF parameters), the relative S^k ($k = 2, 4, 6$) and total S^T CF strength parameters have also been calculated; see corresponding definitions[39] at the bottom of Table 2. These S^2, S^4, and S^6 rotational invariants of the CF represent the short-, mid-, and long-range CF strengths, respectively, in connection with the spatial expansion of CF effects.

The optimization of fits between observed and calculated Stark levels was carried out for each R-doping cation by minimizing the root-mean square function σ; see the bottom of Table 2 for definition, using the program IMAGE.[40]

VI. Results and Discussion of Systematic Trends in the Phenomenological CF Modeling

Initially, the analysis of experimental data was performed independently for each R^{3+} configuration, varying all FI and CF parameters whose values could be properly established from the available data. The results allowed identifying general trends (i.e., order of magnitude and sign) in the evolution of these parameters along the R^{3+} series. The subsequent imposition of some restrains, during the first cycles of the new fitting process, trying to preserve these observed systematic trends in the values of certain parameters, was achieved with no significant change or deterioration in the goodness of phenomenological fits of energy levels. On the other hand, some FI parameters, γ, T^2, and T^8 were held fixed since energy levels which define their values were not observed, and others, M^k and P^i, were constrained to vary within an established ratio.[41]

Apart from possible misinterpretations of experimental data, mainly as a consequence either of missed expected energy levels or due to confusions with secondary phases, among the various $4f^N$ configurations presenting groups of energy levels with experimental/calculated differences systematically higher than the average values,[42] only for Pr^{3+} ($4f^2$) and Nd^{3+} ($4f^3$) have misbehaving energy levels, namely, $^1D_2$ and $^2H(2)_{11/2}$, respectively, been detected. So, though the above-described one-electron CF approximation is usually efficient for a large part of R^{3+} compounds, these indicated discrepancies provide information betraying higher order effects. Improvements regarding the non-negligible mixing with levels of the excited $4f^{N-1}5d^1$ configuration could be included in the CF adjustment to account for these poorly fitted energy levels, and in this way, two-electron CF interactions (correlated CF) have been considered through

(37) Porcher, P.; Couto dos Santos, M.; Malta, O. *Phys. Chem. Chem. Phys.* **1999**, *1*, 397.
(38) Carnall, W. T.; Goodman, G. L.; Rajnak, K.; Rana, R. S. *J. Chem. Phys.* **1998**, *90*, 3443.
(39) Chang, N. C.; Gruber, J. B.; Leavitt, R. P.; Morrison, C. A. *J. Chem. Phys.* **1982**, *76*, 3877.
(40) Porcher, P. Fortran routines REEL and IMAGE for simulation of d^N and f^N configurations involving real and complex crystal field parameters, 1989, see for example: Cascales, C.; Antic Fidancev, E.; Lemaitre Blaise, M.; Porcher, P. *J. Phys.: Condens. Matter* **1992**, *4*, 2721.
(41) Crosswhite, H. M.; Crosswhite, H. *J. Opt. Soc. Am.* **1984**, *1*, 246.
(42) Garcia, D.; Faucher, M. Crystal-field in non-metallic (rare-earth) compounds. In *Handbook on the Physics and Chemistry of Rare Earths*; Gschneidner, K. A., Jr., Eyring, L., Eds.; Elsevier Science: Amsterdam, 1995; Vol. 21, p 263.

Table 2. Free-Ion and Crystal-Field Parameters (cm^{-1}) for R^{3+} in $BiY_{1-x}R_xGeO_5$ Compounds

	Pr	Nd	Sm	Eu	Tb	Dy	Ho	Er	Tm	Yb
E^0	9854(2)	23445(1)	46120(1)			55286(1)	47755(1)	34980(1)	17574(1)	4686(2)
E^1	4563(3)	4712(1)	5199.0(3)			6142(2)	6390.3(3)	6529.8(7)	6660(2)	
E^2	22.82(4)	22.37(2)	25.13(1)			30.56(2)	32.12(2)	32.48(2)	33.79(2)	
E^3	454.8(1)	477.70(9)	508.36(7)			623.63(8)	637.9(7)	659.31(8)	673.6(2)	
a	17.84(5)	17.81(5)	18.81(3)			18.31(3)	16.53(3)	19.04(3)	17.25(6)	
b	−605(6)	−527(5)	−637(2)			−616(2)	−679(2)	−590(3)	−651(1)	
g	[1400]	[1450]	[1625]			[1790]	[1790]	[1790]	[1810]	
z	785(1)	892.6(8)	1161.6(8)			1894.40(8)	2144.0(5)	2358.3(8)	2636.9(8)	2885(1)
$M^{0,a}$	3.25(6)	4.62(9)	3.16(4)			3.9(4)	3.9(4)	6.5(4)	4.0	
$P^{2,b}$	180(13)	450(17)	540(9)			565(9)	906(8)	980	650	
T^2		[260]	[370]			[350]	[375]	[375]		
T^3		26(3)	32(6)			30(3)	49(2)	33(2)		
T^4		6(3)	15(4)			99(2)	123(2)	110(3)		
T^6		−334(8)	−320(9)			−320(11)	−265(13)	−367(13)		
T^7		[400]	288(15)			316(14)	314(15)	413(12)		
T^8		[380]	[362]			[360]	[340]	[300]		
B_0^2	371(18)	365(33)	493(23)	380(20)	386(18)	195(26)	242(34)	285(32)	247(15)	215
B_2^2	187(14)	137(36)	343(17)	118(12)	136(13)	164(15)	245(21)	146(23)	13(11)	−275
B_0^4	−1299(35)	−1264(58)	−1153(51)	−1027(28)	−1039(34)	−1126(44)	−895(39)	−1325(41)	−1574(22)	−1343
B_2^4	−208(50)	−287(57)	215(50)	81(48)	101(38)	366(48)	175(38)	618(37)	430(22)	655
S_2^4	437(41)	964(39)	−621(47)	−586(28)	−740(32)	−839(38)	−530(32)	−487(57)	−492(29)	−490
B_4^4	1(63)	−43(76)	−564(40)	−1045(15)	−1109(22)	−986(29)	−1195(22)	−1033(24)	−387(28)	−472
S_4^4	−1001(26)	−1125(33)	−432(70)	−347(43)	−297(47)	−256(63)	−189(74)	−310(45)	−444(25)	−310
B_0^6	−211(48)	−200(88)	−352(68)	216(33)	86(48)	159(68)	92(50)	210(49)	402(29)	260
B_2^6	−162(70)	−15(74)	239(57)	221(50)	185(48)	148(67)	118(66)	236(39)	343(40)	290
S_2^6	784(38)	285(76)	132(57)	230(25)	40(33)	249(58)	368(30)	175(43)	3(36)	175
B_4^6	−1067(35)	−1249(34)	−1145(31)	−765(25)	−430(38)	−390(45)	−427(27)	−307(30)	−341(29)	−298
S_4^6	−387(52)	−370(76)	−280(64)	−160(63)	−466(36)	−741(39)	−254(47)	−326(40)	−308(27)	−325
B_6^6	−191(44)	−230(63)	−106(77)	−350(38)	−173(40)	−240(48)	−26(32)	−190(39)	173(35)	240
S_6^6	−7(66)	−74(65)	240(56)	−126(34)	4(40)	−53(48)	191(28)	4(46)	226(27)	5
$S^{2,c}$	204	185	222	185	193	134	189	157	111	199
S^4	681	827	597	681	749	747	695	769	669	648
S^6	554	534	496	366	269	363	260	230	275	248
S^T	520	578	466	459	473	486	442	472	422	417
L	34	65	111	29	39	89	101	66	52	7
σ^d	12.7	17.9	18.8	5.9	11.1	17.7	13.0	10.6	13.1	5.7
d_m	8.1	14.9	17.1	4.4	9.1	15.7	11.6	9.1	10.6	4.8
R[e]	1945.1	14465.1	32565.0	562.8	3206.0	21933.2	13609.6	5484.2	5876.1	160.5

[a] M^0, M^2, and M^4 were constrained by the ratios $M^2 = 0.5625M^0$, $M^4 = 0.3125M^0$. [b] P^2, P^4, and P^6 were constrained by the ratios $P^4 = 0.75P^2$, $P^6 = 0.50P^2$. [c] $S_k = \{1/(2k+1)\,[(B_o^k)^2 + 2\sum_q[(B_q^k)^2 + (S_q^k)^2]]\}^{1/2}$ $S_T = [\frac{1}{3}\sum_k S_k^2]^{1/2}$; [d] $\sigma = [\sum(\Delta_i)^2/(L - p)]^{1/2}$, $\Delta = E_o\text{-}E_c$ L number of Stark levels, p number of parameters; [e] $R = (\sum|E_{exp} - E_{cal}|^2)$. Values in parentheses refer to the estimated standard deviation in the indicated parameter. Values in square brackets were not allowed to vary in the parameter fitting.

spin and orbitally correlated CF models[43−47] as well as with models considering the influence of interconfigurational interactions,[48] including odd terms in the expansion of the CF Hamiltonian, also taken into account in the phenomenological simulation of the electric dipole transition intensities,[49] through third-order perturbation terms.[50,51] In practice, these assumptions are difficult to handle because of the larger secular determinant, i.e., the large number of parameters that are required to represent the various two-electron operators that must be added to the CF Hamiltonian, vs the scarcity of observed energy levels, and often the reproduction of experimental splittings are far from being satisfying.

In fact, most of the experimental Pr^{3+} energy level diagrams result in not being accurately described with a classical one-electron CF approximation, as in the current case, with overall experimental and calculated splittings for $^1D_2$ of 836 and 520 cm^{-1}, respectively; see Table A1, Supporting Information. Experimental limitations imposed by the reduced number of experimentally observed energy levels for Pr^{3+} in $BiY_{0.65}Pr_{0.35}GeO_5$ restrict the current fit to the one-electron part of the CF Hamiltonian, and then the five observed $^1D_2$ energy levels are not included in the parametric scheme.

For Nd^{3+} in $BiY_{0.65}Nd_{0.35}GeO_5$ the initial adjustment also yielded the usual bad reproduction of $^2H(2)_{11/2}$, with a calculated splitting of 126 cm^{-1} while the experimental one amounts to 255 cm^{-1}. This phenomenon is known to be more prominent as the fourth-order CF parameters are stronger with respect to second- and sixth-order parameters,[52,53] and this is the current situation. Some empirical corrections have been proved to successfully reproduce the $^2H2_{11/2}$ sequence.[54]

(43) Judd, B. R. *Phys. Rev. Lett.* **1977**, *34*, 242.
(44) Judd, B. R. *J. Phys. C: Solid State Phys.* **1989**, *13*, 2695.
(45) Judd, B. R. *J. Lumin.* **1979**, *18/19*, 604.
(46) Crosswhite, H.; Newman, D. J. *Phys. Status Solidi B* **1984**, *126*, 381.
(47) Yeung, Y. Y.; Newman, D. J. *J. Chem. Phys.* **1987**, *86*, 6717.
(48) Kornienko, A. A.; Dunina, E. B.; Yankevich, V. L. *Opt. Spectrosc.* **1995**, *79*, 700.
(49) Judd, B. R. *Phys. Rev.* **1962**, *127*, 750.
(50) Garcia, D.; Faucher, M. *J. Phys. Chem.* **1989**, *91*, 7461.
(51) Kornienko, A. A.; Dunina, E. B.; Kaminskii, A. A. *J. Exp. Theor. Phys.* **1999**, *89*, 1130.
(52) Faucher, M. Garcia, D.; Derouet, J.; Caro, P. *J. Phys. France* **1989**, *50*, 219.
(53) Faucher, M.; Garcia, D.; Porcher, P. C. R. *Acad. Sci. Paris II* **1989**, *308*, 603.
(54) Faucher, M.; Garcia, D.; Antic-Fidancev, E.; Lemaitre Blaise, M. *J. Phys. Chem. Solids* **1989**, *50*, 1227.

Among them, the division of the $\langle {}^2H(2)_{11/2}|U^4|{}^2H(2)_{11/2}\rangle$ reduced matrix element by 4 improves the simulation of the $^2H(2)_{11/2}$ splitting for Nd^{3+} in $BiY_{0.65}Nd_{0.35}GeO_5$, now 254 cm^{-1}, almost without changing the CF parameters values, and significantly reduces the residue as well as the rms standard deviation, 17.9 cm^{-1}; see Table A2, Supporting Information.

Final FI and C_2 CF parameters for each R^{3+} in the studied germanate matrix are listed in Table 2. Despite the low point site symmetry of R^{3+} in the host, the simulations have produced energy level sequences that show satisfying accordance with the observed data.

The FI parameters for R^{3+} show a clear smooth increase in the electrostatic interaction as indicated by the Racah E^k parameters, and in the spin−orbit coupling constant, ζ_{4f}, toward the heavier R^{3+} cations, owing to the increasing electron repulsion experienced by the 4f electrons. Trends in the configuration interaction terms α and β are less regular, probably because they are less well-defined. So, for example, the value of α for Pr^{3+}, although within the systematic evolution, is somewhat speculative, given that it is essentially defined by the energy of the very weak $^1I_6$ state, for which only one Stark level has been assigned, and changes in α lead to shifts in the center of gravity of $^1I_6$ with respect to that of $^3P_1$, with little or no effect on the simulated level energies for the rest of the $4f^2$ configuration. In any case these terms do not vary much over the series. The γ parameter has been fixed to customary values[38] for each $4f^N$ configuration, that is, with increasing values along the series. Also in several cases the Judd T^λ parameters describing the three-body configuration interactions have been maintained fixed and close to conventional values since their magnitudes strongly depend on certain levels only. Reasonable strengthened values for heavier R^{3+} of M^k and P^i parameters have been obtained, and in no case negative values for electrostatically correlated spin−orbit terms P^i have resulted.[38]

CF parameters as a function of the number of f electrons are shown in Figure 9a−9d. The CF effect would be expected to weaken over the R^{3+} series with the increased nuclear charge to which the electrons are subjected from Pr^{3+} to Yb^{3+} since the electron orbitals are pulled closer to the nucleus. But apart from the nature of the R^{3+} center, the CF is also affected by the distances and bonding angles that characterize the crystallographic site of R^{3+} in the host. If the observed reduction in unit cell parameters when the ionic radius of R^{3+} is getting smaller, see Table 1, supposes a parallel reduction in some R^{3+}−O distance(s), the short-range CF strength would increase. In the following discussion of the CF evolution trends, it must be reminded that the initial and final configurations correspond to especial conditions: data for the larger $Pr^{3+}(4f^2)$ and $Nd^{3+}(4f^3)$ ions are derived from doped materials, while remaining CF analyses have been performed in R^{3+} stoichiometric compounds, and the indicated values for Yb^{3+} are not the result of a true energy level fit, but they are derived from tests that starting with previous data of Er^{3+} and Tm^{3+} provide an adequate simulation of the experimental energy levels.

As shown in Figure 9a, an evolution to lower magnitudes can describe the general behavior of B_0^2 from $4f^2$ to $4f^{13}$

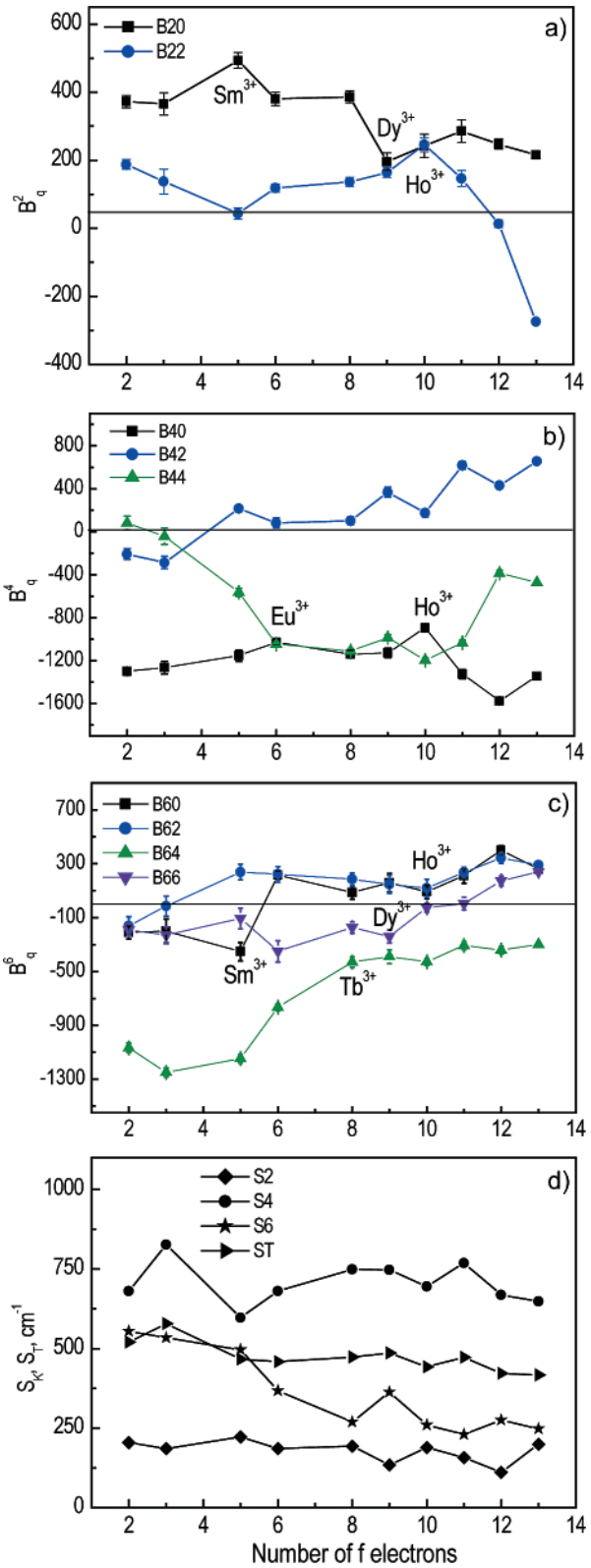

Figure 9. Variation of (a) short-, (b) mid-, and (c) long-range crystal-field parameters and crystal-field strengths (d) as a function of the number of f electrons for R^{3+} in $BiRGeO_5$ or $BiY_{1-x}R_xGeO_5$.

configurations, in accordance with the above nuclear charge increase criterion. This trend is especially clear from Sm^{3+} ($4f^5$) to Dy^{3+} ($4f^9$). Beyond the minimum value for Dy^{3+} B_0^2 regains strength, but holds up the decreasing trend from Er^{3+} ($4f^{11}$) to Yb^{3+} ($4f^{13}$). The observed discontinuity at the beginning of the series for Pr^{3+} and Nd^{3+} could be related

to the more reduced size of the unit cell of $BiYGeO_5$ in which they are embedded, which may hinder the comparison. Similar regions, previous to Sm^{3+}, among Sm^{3+} and Ho^{3+}, and beyond Ho^{3+}, can be distinguished in the evolution of B_2^2 values, and up to Dy^{3+} they are going in the opposite direction with regard to B_0^2. The CF strength parameter S^2, a quantitative measure of the short-range CF interactions, smoothes to some extent these opposite effects, and thus evolves in a slightly decreasing way across the series, although obviously the strong negative B_2^2 value for Yb^{3+} raises it.

Among midrange B_q^4 CF parameters, Figure 9b, for B_0^4 ones, all of them with negative values, Ho^{3+} marks the inflection point; i.e., after a slight growth from the beginning of the series, the values for Er^{3+} and Tm^{3+} clearly drop. Variations in B_2^4 parameters are stronger and evolve with a clear definition to higher values across the series; however, it is worth to mention that although Pr^{3+} and Nd^{3+} are well in accordance with the observed trend, they hold *negative* values with medium magnitudes. Also negative B_4^4 parameters essentially lessen up to Ho^{3+}, and then go up for Er^{3+}, Tm^{3+}, and Yb^{3+}. Taking into account all these individual behaviors, the S^4 plot shows a rather erratic aspect, with the maximum value for Nd^{3+} followed by the minimum one for Sm^{3+}.

A well-defined increase of CF parameters B_0^6 from Sm^{3+} and B_6^6 from Dy^{3+} to the end of the series is observed in Figure 9c. After a marked increase of all *negative* B_4^6 values after Nd^{3+}, they remain nearly constant for the second half of the series, from Tb^{3+} to Yb^{3+}. In contrast, no important variations can be observed for B_2^6 CF parameters, the lowest value corresponding to Ho^{3+}, with higher values for configurations toward the left and right sides. The long-order CF strength S^6 plot results in a clear negative slope from Pr^{3+} to Tb^{3+} and is almost constant for heavy ending Ho^{3+}—Yb^{3+} configurations. The overall CF strength S^T, which accounts for all CF parameters and describes the total CF strength, shows only a slight decreasing trend along the series, although for left and right neighboring cations to Ho^{3+} some regaining of S^T magnitude is depicted.

In summary, apart from the mentioned inflection point that plots of many B_q^k parameters have for Ho^{3+} (for which although the current fit is good and even better than for other $4f^N$ configurations, the ratio between observed energy levels and total levels for $4f^{10}$ is probably not adequate enough), the only noticeable discontinuity observed is for B_4^6 going from Sm^{3+} to Tb^{3+}. It has been repeatedly interpreted[38,45] as an indication of the need to include two-electron operators in the CF Hamiltonian. However, their effects seem to be rather small[55−57] and the importance of this mechanism has not been clearly established. Also, a decrease in the energy of excited configurations of opposite parity, for example, $4f^N$−$5d^1$, which occurs at the middle of the R^{3+} series,[58] should strengthen the CF effect by increasing the mixture of the opposite parity terms of the 4f wave functions.

VII. Conclusions

We have satisfactorily correlated the sequences of low temperature observed energy levels of R^{3+} in $BiY_{1-x}R_xGeO_5$ ($0 < x \leq 1$ for R = Sm to Yb, $x \leq 0.35$ for Pr or Nd) with consistent sets of free-ion and C_2/C_s CF parameters. Systematic trends in the values of these parameters along the R^{3+} series have been outlined in order to establish further comparisons with corresponding $4f^N$ configurations in other available solid hosts. The variation of the CF parameters is such that the direct extrapolation from the start to the end of the R^{3+} series can lead to inaccuracies in their estimation, even if the structure does not change. No distortions in the local environment of the R^{3+} have been detected, excluding possible substitutions with Bi^{3+} in the R^{3+} point site.

This new orthorhombic germanate host accepts large amounts of the optically active R^{3+} ions, up to the full R^{3+} stoichiometry for the smaller ones, which constitutes an interesting prospect regarding possibilities for size reduction of optical systems. Focusing on Yb^{3+}, the crystal-field interactions that it experiences in $BiYbGeO_5$ lead to an observed splitting of $\sim$660 cm^{-1} for the $^2F_{7/2}$ ground state, and such a medium-high splitting is a prerequisite for an efficient Yb quasi-three-level laser operation. In fact, this splitting has a similar value to that reported for Yb-doped $LiNbO_3$, and superior to that observed in Yb-doped $YAl_3(BO_3)_4$, $YAlO_3$, $LiYF_4$,[59] ordered double tungstate $KYb(WO_4)_2$,[60] and in recently described disordered Yb-doped double tungstate $NaGd(WO_4)_2$,[61] $NaLa(WO_4)_2$,[62] and molybdate $NaLa(MoO_4)_2$,[62,63] all of them well-known laser crystal hosts. Finally, $BiYbGeO_5$ also possesses intense Raman modes with high-frequency shifts, adequate for efficient stimulated Raman scattering SRS lasing.[64]

More efforts are required to assess the suitability of these materials for laser operation, and initially they should consider the development of adequate crystal growth procedures.

Acknowledgment. The authors acknowledge the financial support through the Spanish projects MAT2002-04603-C05-05 and CAM MAT/0434/2004.

Supporting Information Available: Ten additional tables. This material is available free of charge via the Internet at http://pubs.acs.org.

CM060785T

(55) Crosswhite, H.; Newman, D. J. *J. Chem. Phys.* **1984**, *81*, 4959.
(56) Jayasankar, C. K.; Richardson, F. S.; Reid, M. F.; Porcher, P.; Caro, P. *Inorg. Chim. Acta* **1987**, *139*, 287.
(57) Cascales, C.; Zaldo, C.; Caldiño, U.; García Solé, J.; Luo, Z. D. *J. Phys.: Condens. Matter* **2001**, *13*, 8071.
(58) Brewer, L. *J. Opt. Soc. Am.* **1971**, *61*, 1666.
(59) Auzel, F. *J. Lumin.* **2001**, *93*, 129.
(60) Klopp, P.; Griebner, U.; Petrov, V.; Mateos, X.; Bursukova, M. A.; Pujol, M. C.; Solé, R.; Gavalda, J.; Aguiló, M.; Guëll, F.; Massons, J.; Kirilov, T.; Diaz, F. *Appl. Phys. B* **2002**, *74*, 185.
(61) Rico, M.; Liu, J.; Griebner, U.; Petrov, V.; Serrano, M. D.; Esteban-Betegón, F.; Cascales, C.; Zaldo, C. *Opt. Express* **2004**, *12*, 5362.
(62) Rico, M.; Liu, J.; Cano-Torres, J. M.; García-Cortés, A.; Cascales, C.; Zaldo, C.; Griebner, U.; Petrov, V. *Appl. Phys. B* **2005**, *81*, 621.
(63) Liu, J.; Cano-Torres, M.; Cascales, C.; Esteban-Betegón, F.; Serrano, M. D.; Volkov, V.; Zaldo, C.; Rico, M.; Griebner, U.; Petrov, V. *Phys. Status Solidi A* **2005**, *202*, R29.
(64) Basiev, T. T.; Sobol, A. A.; Zverev, P. G.; Osiko, V. V.; Powell, R. C. *Appl. Opt.* **1994**, *38*, 594.